Advanced Materials Technologies

ADVANCED MATERIALS TECHNOLOGIES
www.advmattechnol.com

RESEARCH ARTICLE

High-Performance Neuromorphic Visual System With Image Pre-Processing via Normally-Off GaN MOS-HEMT

Ge Yang[1] | Haitao Du[1] | Haolan Qu[1] | Changshu Liu[1] | Yudong Li[1] | Xuanling Zhou[1] | Hongzhi Wang[2] | Kerui Li[2] | Xinbo Zou[1]

[1]School of Information Science and Technology, ShanghaiTech University, Shanghai, China | [2]College of Materials Science and Engineering, Donghua University, Shanghai, China

Correspondence: Xinbo Zou (zouxb@shanghaitech.edu.cn)

Received: 13 February 2026 | **Revised:** 22 May 2026 | **Accepted:** 9 June 2026

Keywords: GaN MOSHEMTs | image preprocessing | number recognition | optoelectronic synaptic devices | visual neuromorphic system

ABSTRACT

This study presents a novel image processing and recognition system enabled by an enhancement-mode recessed-gate GaN MOSHEMT artificial synapse. By leveraging trap modulation near the AlGaN/GaN heterojunction, long-term potentiation and long-term depression characteristics were well demonstrated, ensuring high linearity and symmetry required for neural computing. Upon being implemented in an artificial neural network, this approach achieves a recognition accuracy of 98.27% on the MNIST dataset of handwritten digits. Additionally, an image compression preprocessing scheme capable of ultra-high compression ratio is implemented based on the photoelectric conversion and memory capabilities, thereby significantly enhancing transmission efficiency. This work demonstrates a promising approach for developing comprehensive signal-processing systems that include sensing, storage, and computing, paving the way for advanced human-machine interaction and visual neuromorphic technologies.

1 | Introduction

In an era of explosive development in Artificial Intelligence, the intelligent information processing technologies designed to solve complex problems and execute human-like tasks have attracted widespread interest [1–3]. However, current computational architectures face significant challenges regarding processing speeds and energy consumption, known as the Von Neumann bottleneck [4]. Neuromorphic computing has emerged as an increasingly attractive solution by simulating the biological neural system [5–8]. The structure is capable of massive data selection and parallel computing, drastically improving operational efficiency [7, 9]. Serving as a fundamental weight-processing component in neuromorphic systems, the artificial synapse concurrently realizes persistent photo-conductivity and synaptic plasticity, playing a pivotal role in determining computational performance [10–12].

To advance neuromorphic computing, sufficient effort has been invested in the research and development of artificial synapses, specifically aimed at achieving enhanced weight modulation ability. Long-term potentiation (LTP) and long-term depression (LTD) behaviors—which mimic biological neural plasticity—are primarily applied in modulation processes [13]. In previous studies, these characteristics were widely utilized to realize parallel storage and computing of layer-to-layer weight transition within artificial neural network (ANN) [14–16]. Crucially, the nonlinearity of LTP and LTD are the dominant factors for the network training performance, which exert a significant influence on aliasing between different weight levels, thereby determining high recognition accuracy [17–20]. By leveraging trap modulation, the GaN device can achieve stable and robust weight modulation process [21, 22]. Furthermore, the recessed gate can enable a normally-off operation mode, minimizing the static energy consumption and simplifying the driving circuit [23–25]. These device properties provide notable advantages for realizing high-performance neural network computing.

Moreover, the optoelectronic synaptic devices exhibit great potential to form an entire neuromorphic system involving sensing, processing and storage. In addition to the weight modulation function mentioned before, synaptic devices possessing visual preprocessing ability to transform and organize raw visual information may lead to improved transmission efficiency and processing speed [7, 12, 26]. Previous research has successfully constructed pattern detection and compression methods based on the optoelectronic response of synaptic devices [27, 28]. However, the ultra-high compression ratio method based on a synaptic device has yet to be realized due to demands for image feature extraction for subsequent training [29–31]. Based on the direct energy bandgap, high electron mobility, and inherent stability of gallium nitride, the GaN synapses will effectively enhance the pattern detection capabilities [32–34]. The capability for photoelectric conversion and long-term memory also enables multi-pixel processing and compression application. Consequently, the GaN MOSHEMT synapse shows great potential for a high-ratio compression scheme with excellent feature extraction quality. Integrating the preprocessing, calculation and storage functions into a single GaN-based synaptic device, it can effectively minimize the circuit complexity and source consumption.

In this work, we proposed an optoelectronic artificial synaptic device based on a recessed-gate GaN MOSHEMT. Utilizing trap modulation of the interface state, synaptic plasticity is emulated under optical stimuli, including excitatory postsynaptic current (EPSC), paired-pulse facilitation (PPF), spike-number-dependent plasticity (SNDP), spike-frequency-dependent plasticity (SFDP), and short-term memory (STM) to long-term memory (LTM) transition. To reduce the energy consumption of GaN MOSHEMT, we have achieved a normally-off operation under light illumination. Moreover, LTD/LTP characteristics are applied to realize storage and calculation functions in the training procedure of ANN, achieving a high digit image recognition accuracy of 98.27%. An SNDP-based image compression up to 28 times ratio is constructed to reduce transmission redundancy. Noise effects and low-illumination conditions were investigated to demonstrate its stability across various environments. Conclusively, a power-efficient comprehensive neuromorphic system implementing sensing, storage and computing is demonstrated through a GaN MOSHEMT synaptic device, expanding the further development of biology-inspired systems.

2 | Results and Discussion

2.1 | Device Fabrication and Characterization

This study investigates a three-terminal synaptic device based on a recessed-gate GaN MOSHEMT. The device comprises an AlN/GaN-based buffer layer, a 210 nm i-GaN channel layer, a 0.1 nm AlN spacer layer, a 23 nm AlGaN barrier layer, and a 2 nm GaN cap layer. The heterojunction was epitaxially grown on a 6-inch Si substrate using metal–organic chemical vapor deposition (MOCVD). After mesa isolation, the AlGaN layer beneath the gate electrode is etched thinner through neutralized beam etching (NBE) to achieve higher gate control ability and normally-off operation mode. The NBE is performed by incident low-energy argon ions of 200 eV with a nominal etching rate of 3.5 nm/min and etching time of 6 min and 15 s, which can effectively reduce surface roughness and mitigate etching damage [25, 35]. Ohmic contacts were formed by depositing Ti/Al/Ni/Au (20/150/50/80 nm) in source and drain regions, followed by rapid thermal annealing at 870°C for 30 s in an N_2 ambient. Subsequently, an Al_2O_3 dielectric layer with a thickness of 15 nm was deposited by plasma-enhanced atomic layer deposition (PEALD) at 300°C. Finally, Ni/Au (20/200 nm) was used as gate metal and contact pads on the top of dielectric layer. The gate length L_g, gate-source distance L_{gs}, gate-drain distance L_{gd}, and gate width W_g of the devices were 1, 2, 10, and 20 µm, respectively.

2.2 | Synaptic Characteristics

Figure 1a illustrates the structural comparison between the proposed device and a prototypical biological synapse. In the biological nervous system, synapses are fundamental components that enable efficient signal transfer between neurons. With stimulation of the pre-synaptic terminal, the membrane triggers the release of neurotransmitters into the synaptic cleft via exocytosis. These neurotransmitters then activate receptors on the post-synaptic membrane to open ion channels, facilitating signal transmission. The connection strength between neurons is described as synaptic weight, which is used to characterize the biological communication function [10, 36]. In the AlGaN/GaN MOS-HEMT device, these biological elements are emulated by the gate electrode (pre-synapse), the two-dimensional electron gas (2DEG) channel (post-synapse), and the drain-to-source current (post-synaptic current). In Figure 1b, the physical structure of the device is captured via Scanning Electron Microscopy (SEM). Figure 1c displays the transfer characteristics of the device through adding gate voltage V_{gs} sweep (from −3 to 5 V) with varying drain voltage V_{ds} (from 0.5 to 2.5 V with 0.5 V steps). When V_{ds} is 0.5 V, the threshold voltage is measured to be 0.8 V, confirming the device's normally-off operational state. Figure 1d shows the output characteristics, where the drain current I_{ds} grows linearly before reaching saturation as V_{ds} is swept from 0 to 8 V (with V_{gs} ranging from 1 to 4 V).

In the experiments, photoexcitation serves as the input stimulus, photogenerated carriers act as synaptic neurotransmitters, and the drain current functions to facilitate carrier transport. Unlike typical optoelectronic GaN synaptic devices that require specific gate bias to maintain an off-state during testing, these enhancement-mode GaN MOS-HEMTs possess a threshold voltage V_{th} significantly above 0 V. Consequently, at a gate bias of V_{gs} = 0 V, the device remains inherently in the off-state with an exceptionally low leakage current of 0.15 µA/mm (at V_{ds} = 0.5 V). This characteristic eliminates the need for a holding voltage, significantly reducing energy consumption. Figure 1e depicts the entire process of a single EPSC event, including

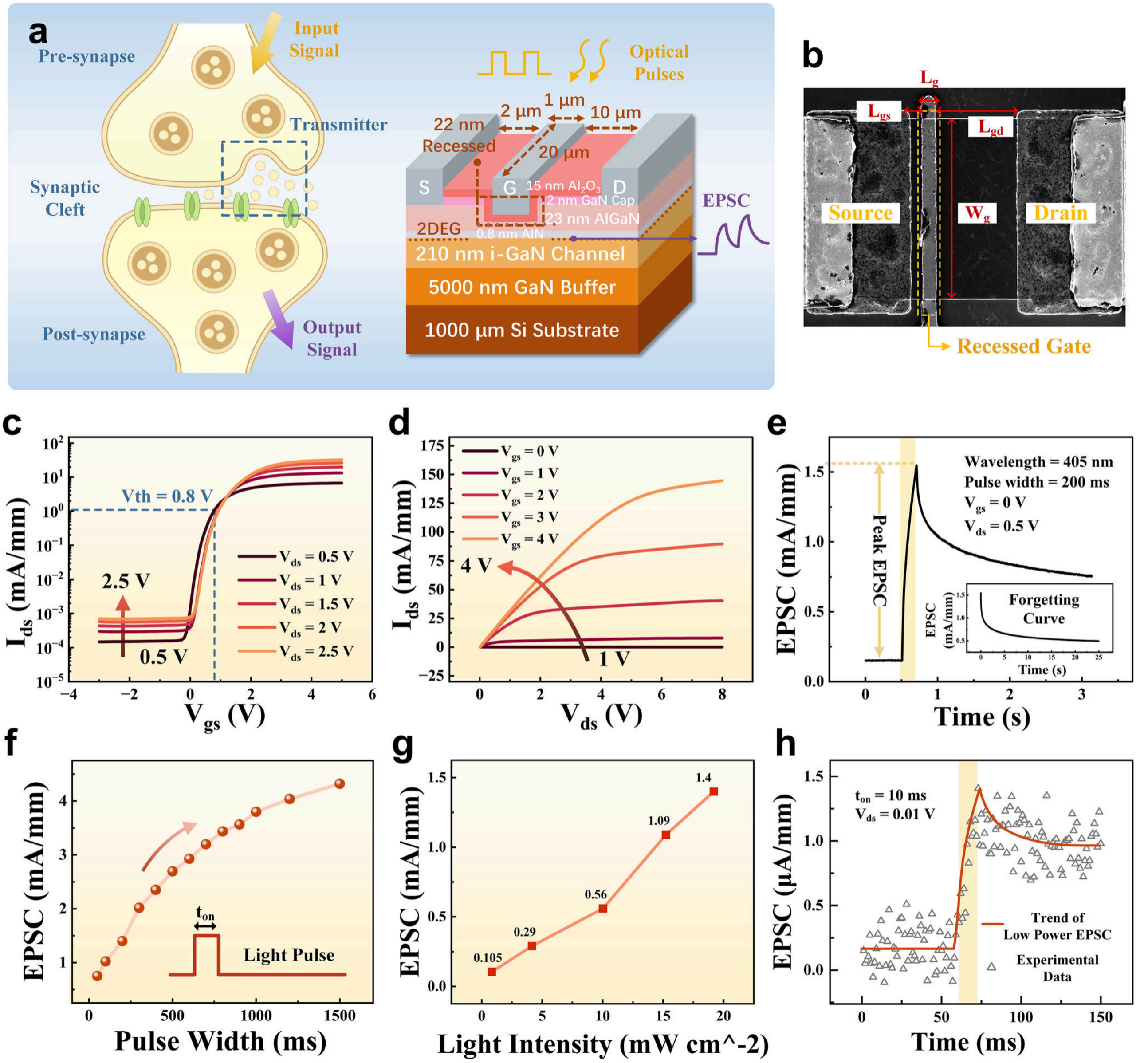

FIGURE 1 | (a) Schematic of the biological synapse and structure of the synaptic device. (b) SEM of the GaN synaptic device. (c,d) show the transfer and output characteristics, respectively. (e) Excitatory postsynaptic current under a single 200 ms optical pulse, with gate voltage of 0 V and drain voltage of 0.5 V. (f) Peak EPSC value as a function of optical pulse width. (g) EPSC responses with different incident light intensity (200 ms, 0.5 V). (h) Low power event triggered by a single optical pulse (10 ms, 0.01 V).

both the generation of current and subsequent decay curve. This event was triggered by a 405 nm light pulse with a duration of 200 ms and an intensity of 19.19 mW/cm^2, with gate and drain biases set at 0 and 0.5 V, respectively. Upon the optical excitation, optoelectronic carriers are generated by the device and then injected into the 2DEG channel between the AlGaN/GaN heterojunction, triggering the fast rise of the current. During the same time, part of the carriers are captured by interface states of the dielectric layer. After the termination of optical excitation, these traps slowly release the optoelectronic carriers and induce the gradual decay of the current, which accounts for the short-term memory [23, 37]. The net peak value of the EPSC is measured as 1.40 mA/mm. The repeated EPSCs are consistent with each other, indicating reliable reproducibility, as shown in Figure S1. The optoelectronic response can be modulated through illumination conditions, including changing the pulse duration and light intensity. Increasing the pulse duration brings about a significant increase in the number of light induced carriers, and then enhances the EPSC amplitude, which is shown in Figure 1f. Meanwhile, the GaN device also demonstrates excellent adaptability to varying light intensity conditions, as depicted in Figure 1g.

Energy consumption represents as a vital parameter of evaluating the synaptic performance. Since the operation gate voltage is maintained at 0 V, the energy consumption associated with the gate electrode is negligible. Therefore, the drain current is a primary factor in the overall energy usage. The energy consumption of an optoelectronic synaptic device can be determined using the following formulas [38, 39]:

$$dE_1 = V_{ds} \times I_{ds} \times dt \tag{1}$$

$$dE_2 = P \times S \times dt \tag{2}$$

In Equation (1), I_{ds} is the peak EPSC value and dt denotes the optical pulse duration. From the equation, it can be deduced that shortening the pulse duration and reducing the V_{ds} voltage are effective strategies for lowering the energy consumption of synaptic devices. The equation mainly describes the dynamic energy consumption of a single EPSC event. Figure S2a,b detail the energy consumption of the EPSC events with different optical pulse duration and optical intensity. Specifically, energy consumption can be optimized through changing the optical and electrical conditions. In this case, an optimized energy of mere 16.5 pJ by reducing the pulse duration and V_{ds} to 50 ms, 0.01 V, indicating excellent potential for low-power operation. The experimental data are depicted as hollow points in Figure 1h. In Equation (2), P, S represent the light intensity and active area, while dt relates to the pulse duration. Equation (2) can be applied to calculate the energy consumed by the optical source. Considering the light intensity of 19.19 mW/cm^2 and the same pulse duration of 200 ms, the applied optical power for the device is 9.93 µJ. In comparison, E_1 of the first equation characterizes the electrical response, and E_2 of the second equation characterizes the light absorption of the device [14].

Figure 2a illustrates the memory rules of the artificial synapse. Upon sensing the external information, the synapse initially exhibits a short-term memory characterized by rapid forgetting, while a long-term memory indicates information retention over a prolonged period [40, 41]. The memory development and strengthening can be regulated through modulating the stimulus intensity. These behaviors emulate biological synapses, laying the foundation for realizing weight storage and computing in neuromorphic systems.

In neuroscience, the temporal enhancement of synaptic strength is referred to as short-term potentiation (STP). Paired-pulse facilitation is a typical case of STP, which reflects the ability of biological synapses to process and decode temporal information [42]. PPF typically manifests as: during continuous stimulation, the current response triggered by a subsequent stimulus is greater than the initial response [43]. To emulate this functionality, PPF responses were measured in the AlGaN/GaN synaptic device by applying two sequential optical pulses (200 ms duration, 200 ms interval time Δt). The bias conditions remained consistent with the previous EPSC measurements. As illustrated in Figure 2b, the first peak current (A_1) and second peak current (A_2) are 1.47 and 1.98 mA/mm, respectively. The resulting PPF index, defined as the ratio of A_2 to A_1, is then calculated to be 134.78%, indicating a pronounced enhancement of the excitatory current. Furthermore, the decay of PPF index as a function of the pulse interval (Δt) can be characterized by a double-exponential function [39, 44]:

$$PPF = 1 + C_1 \exp\left(-\frac{\Delta t}{\tau_1}\right) + C_2 \exp\left(-\frac{\Delta t}{\tau_2}\right) \tag{3}$$

where C_1 and C_2 represent the relative magnitudes of the two decay stages, while τ_1 and τ_2 denote the characteristic relaxation times for the first and second spikes, respectively. The fitting curve is shown as a solid line in Figure 2c, with extracted values of $C_1 = 21.15$, $C_2 = 17.40$, $\tau_1 = 0.15$ s, and $\tau_2 = 0.99$ s. The measured PPF index decreases rapidly at short intervals and stabilizes as Δt increases, mirroring biological synaptic behavior. Detailed double-pulse curves with different interval time are shown in Figure S3. As Δt increases from 50 ms to 10 s, the PPF ranges from 144.77% to 113.09%. Mechanistically, the carriers released by the interface states accumulate with those generated by the second pulse, which is the underlying cause of the facilitation. As the interval between the pulses increases, the enhancement effect declines as most carriers have already been released [45]. This characteristic offers a pathway for achieving the modulation of short-term plasticity.

The response current of the GaN-based artificial synapse can be modulated by varying the drain or gate bias. Under conditions of a 200 ms, 405 nm light pulse and a gate voltage of 0.5 V, the EPSC amplitude increases rapidly with V_{ds} and subsequently reaches saturation, as shown in Figure 2d. The total enhancement magnitude of the peak current reached a notable 582.98%. Figure 2e highlights three specific EPSC curves at V_{ds} levels of 0.5, 1.0, and 1.5 V, with corresponding amplitudes of 1.84, 2.43, and 2.62 mA/mm. Similarly, Figure 2f illustrates the relationship between EPSC amplitude to gate bias at a fixed $V_{ds} = 0.5$ V. As V_{gs} increased from −1 to −0.25 V, the excitatory current rose from 0.28 to 1.64 mA/mm, showing significant sensitivity as the gate voltage approached 0 V. This phenomenon is attributed, on the one hand, to the increased participation of photogenerated carriers participating in conduction under high electric fields, and on the other, to changes in the probability of carrier capture or emission induced by the increase in the applied voltage [22, 46]. Collectively, these results confirm that both gate and drain biases can be utilized to fine-tune the performance of recessed-gate AlGaN/GaN MOS-HEMT optoelectronic synapses.

The modulation of synaptic plasticity, specifically the transition from STM to LTM, is achieved through high-intensity optical stimulation, demonstrating the advanced learning capabilities of the GaN MOSHEMT synaptic device. As illustrated in Figure 3a, the potentiation of the synaptic response was characterized by increasing the number of optical pulses from 3 to 30. Each pulse is stimulated with a duration and interval of 200 ms, with the voltage bias held constant as previously described. The application of a three-pulse sequence elicited a short-term response with a relatively low EPSC amplitude of 2.34 mA/mm. Conversely, increasing the stimulus to 30 pulses elevated the EPSC amplitude to 5.08 mA/mm, indicating a strengthening of synaptic weight via repeated stimulation. Figure S4 shows amplitudes of the final EPSC event with varying pulse counts. Figure S2c illustrates energy consumed by these events, revealing the dynamic power consumption under pulsed modulation. Furthermore, the frequency dependence of the EPSC is shown in Figure 3b. When the frequency was increased from 0.2 to 2.5 Hz (with a fixed 10 s total period and 200 ms pulse width), the device exhibited both enhanced response amplitudes and enhanced memory retention. Figure 3d provides a detailed view of this frequency-dependent enhancement, which resulted in a peak current value of 4.57 mA/mm. In Figure 3c, following an

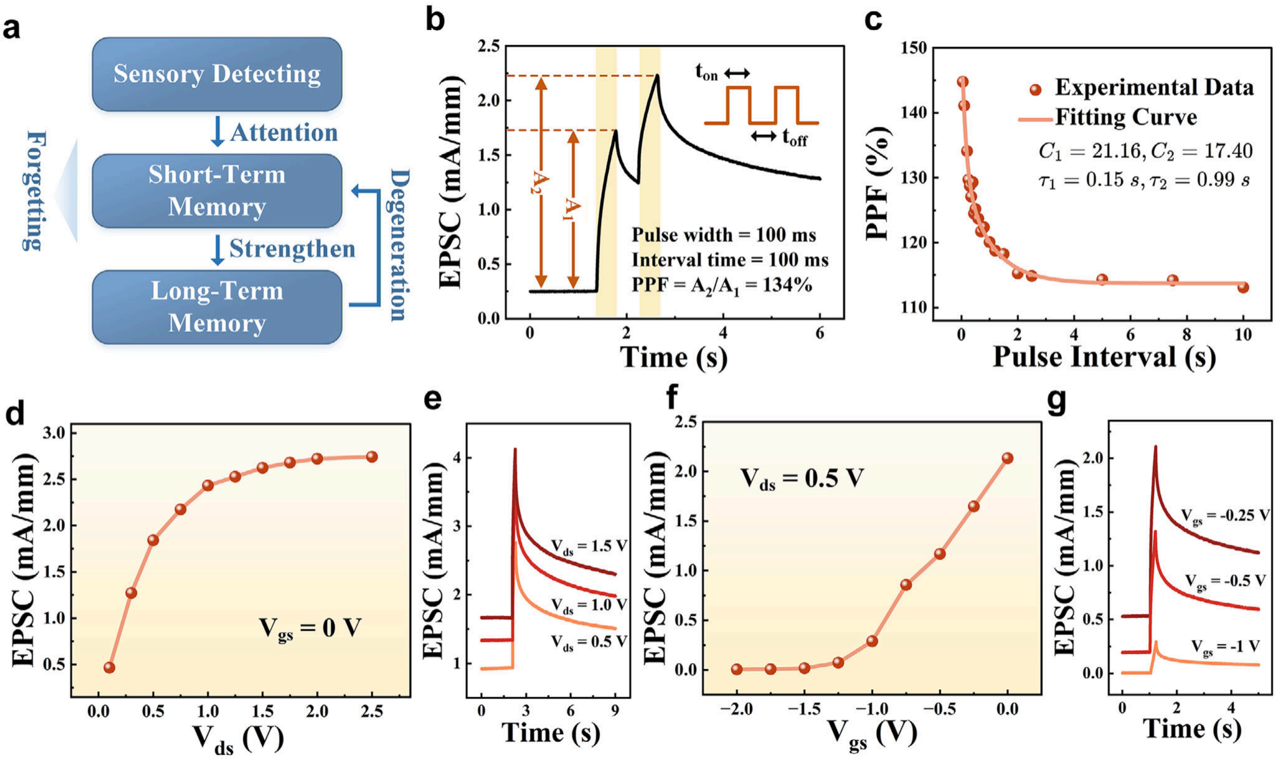

FIGURE 2 | (a) Schematic of the memory procedure of the artificial synapse. (b) Typical PPF response of the recessed-gate AlGaN/GaN MOS-HEMT with adjacent applied pulses. (c) The amplitude of PPF as a function of double-pulse interval between two sequential pulses. (d) Drain voltage dependence of EPSC amplitude with 200 ms optical spike duration and 0 V gate voltage. (e) Complete current response applying V_{ds} from 0.5, 1.0 to 1.5 V. (f) Relationship between peak EPSC to applied gate voltage with 200 ms optical spike duration and 0 V gate voltage. (g) The photocurrent applying V_{gs} of −1, −0.5 and −0.25 V.

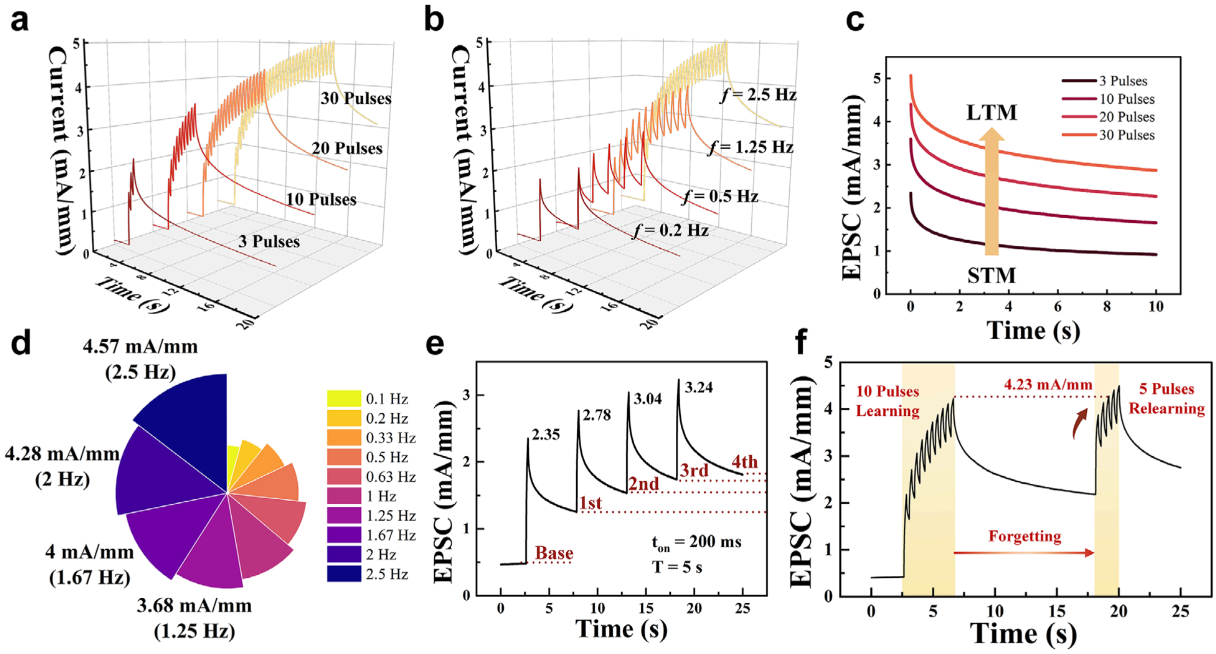

FIGURE 3 | (a) The photocurrent responses of the device under 405 nm light with different pulse numbers (3, 10, 20, and 30). (b) The photocurrent under the simulation of different frequencies (0.2, 0.5, 1.25, and 2.5 Hz). (c) Decay curve for varies times of optical pulse, showing the transition from STM to LTM. (d) The EPSC amplitudes related to optical pulse frequencies varying from 0.1 to 2.5 Hz. (e) The step-learning process is induced by three optical pulses at 3 s intervals. (f) The learning-forgetting-relearning process controlled by 10- to 5 pulses.

increased stimulation intensity, a significant enhancement of the decay current can be observed. This is regarded as evidence for thetransition from STM to LTM. The potentiation of synaptic memory can be attributed to that the carriers are captured by interface states of deeper energy level below conduction band, which has a larger capture/emission time constant. It is these deep-level traps that retain charge carriers for extended periods, thereby enabling long-term storage.

The inherent memory capacity of these synaptic devices can be leveraged to simulate human cognitive functions [47]. Figure 3e demonstrates the advanced synaptic function of "step-learning," revealing the correlation between repetitive learning and memory depth. In this experiment, a 200-ms light pulse was applied within a 5 s cycle and repeated four times. The EPSC displayed four distinct, incremental current levels and successfully maintained stable current levels. This behavior demonstrates the device's ability to integrate and store multiple combinations of information. In Figure 3f, the "Learning-Forgetting-Relearning" function is demonstrated through two distinct groups of stimuli. During the initial 10-pulse "learning" phase, the EPSC increased significantly and reached 4.23 mA/mm. Once the stimulation ceased, the current gradually decayed, mimicking the biological forgetting process. Upon the introduction of a second stimulus group, the current recovered rapidly and exceeded its previous peak within only 5 pulses. The highly efficient relearning behavior suggests that even after a period of forgetting, memory can be rapidly restored and further enhanced through revision. These findings align with the general trend of the Ebbinghaus forgetting curve, illustrating the precise modulation of memory strength over time [48].

Toward a complete neural computing system, the transistors should possess both "writing" and "erasing" capabilities to realize complex learning tasks. Thus, the device should exhibit the property of long-term depression in addition to long-term potentiation function to effectively act as a neural synapse. As shown in Figure 4a, the normalized potentiation/ depression (P/D) characteristics were extracted through 30 consecutive optical pulses (200 ms, 19.19 mW/cm^2, 405 nm) and electrical pulses (200 ms, 0.05 V), respectively. Notably, the memory of the device shows significant depression under the stimulation of a positive gate voltage. As a key factor to evaluate a synaptic device in neuromorphic computing, the nonlinearity ($|NL|$) has significant influence on the computing accuracy. The NL can be calculated with the normalized P/D conductance (G) through the following equations [49]:

$$G_{LTP} = B \cdot \left(1 - \exp\left(-\frac{P}{A_p}\right)\right) + G_{min} \tag{4}$$

$$G_{LTD} = -B \cdot \left(1 - \exp\left(\frac{P - P_{max}}{A_D}\right)\right) + G_{max} \tag{5}$$

$$B = \frac{G_{max} - G_{min}}{1 - \exp\left(-\frac{P_{max}}{A_{P,D}}\right)} \tag{6}$$

G_{LTP}, G_{LTD}, G_{min} and G_{max} are the measured conductances in P/D process and their maximum and minimum values. P and P_{max} are the input pulse number and the maximum number. A and B can be extracted through the fitting of experimental data, where A is a parameter representing the nonlinearity factor, and B is a fitting constant to normalize the conductance range [50, 51]. The calculated A and $|NL|$ of LTP/LTD are listed in Table S1, which also demonstrates high symmetry in the two processes. Meanwhile, to validate the endurance of the device, 30 cycles of potentiation behaviors were plotted in Figure S5. It can be observed that the conductance change can be well controlled, suggesting excellent reproducibility.

Inspired by the structure of human brains, the ANN is established to learn or classify complex models. To demonstrate the potential of GaN synaptic devices in neuromorphic networks, we constructed an ANN based on a supervised learning multilayer perceptron with the backpropagation algorithm to realize visual recognition. The memory and modulation of the synaptic weight matrices W_{IH} and W_{HO} between different neuron layers were realized by the LTP and LTD characteristics of the synaptic device. As shown in Figure 4b, the synaptic weight was expressed as $W = G^{+}—G^{-}$, where G^{+} and G^{-} can be implemented through the LTP/LTD curves and remain positive values [52]. Figure 4c depicts the weight transfer process, where the input neurons were multiplied with the synaptic matrix and then summed up. The overall architecture of the ANN recognition network is shown in Figure 4d. The network utilized 28 × 28 pixels handwritten numbers from MNIST, which consists of 60 000 images for training and 10 000 images for testing [53, 54]. The applied images are shown in Figure S4. The ANN architecture consists of 728 input neurons (corresponding to the image dimensions), 256 hidden neurons, and 10 output neurons. A ReLU activation layer and a dropout layer were added between layers to adapt to nonlinear models and avoid overfitting. After activation, the information was transferred to the neurons in the next layer. During backpropagation, gradient descent and the Adam optimizer were applied to update the synaptic weights. Network performance was evaluated by comparing the output classification against ground-truth labels.

For the neural network, it exploits the synaptic plasticity to realize weight modulation of the layer-to-layer transition in the neural network. While the LTP/LTD provided equitable distribution of synaptic weight and determined the relationship between the optical/voltage input and current output, it also restricted the range of weight change. As displayed in Figure 4e,f, in the first epoch, the confusion matrix has numerous instances of incorrect label classification, however, as the number of epochs increased, the error classification gradually decreased. With this method, the accuracy of hardware-based image recognition reached a high level of 98.27% after 50 epochs of training, approaching the accuracy of a basic ANN, as shown in Figure 4g. This high accuracy demonstrates the superiority of the synaptic device in ANN networks.

The proposed synaptic device also possesses optical preprocessing abilities, demonstrating significant potential for comprehensive neuromorphic computing. The entire schematic for the preprocessing process is displayed in Figure 5a. The implementation of pattern detection and multi-ratio compression relies on the

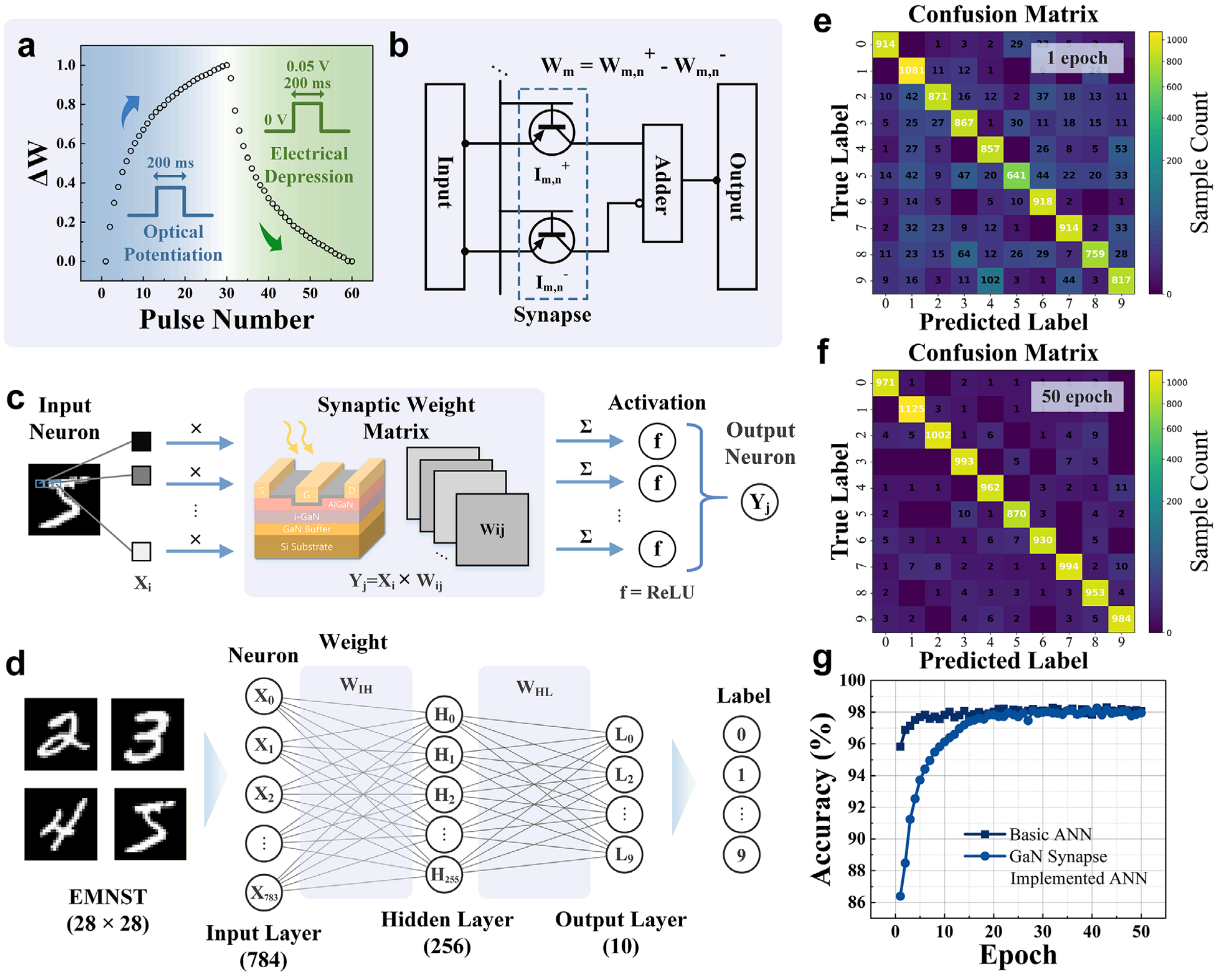

FIGURE 4 | (a) LTP and LTD characteristic curve of the synaptic device by electron pulse. (b) Schematic of synaptic modulation for the neural network. (c) The weight transfer procedure utilizing artificial synapse. (d) Schematic Diagram of the image recognition process based on ANN neuromorphic computing. (e,f) shows the confusion matrix at the first epoch and the final epoch. (g) Recognition accuracy as a function of the epoch for basic ANN and synaptic device modulated ANN with 50 training epochs.

mapping from optical pulses to EPSC values, as shown in Figure 5c. Using 4× compression as an example, the system first received a binarized image as input. Every four consecutive pixels in a row were treated as an independent region. The count of bright pixels within each region was mapped to a specific output brightness level, determined by the EPSC response to a sequence of optical pulses. These mapping rules are derived from the EPSC values under 28 consecutive optical pulses. For 4× compression, specifically, only the first five normalized spikes are utilized, while for 28× compression, all points are applied. Through this approach, an initial 28 × 28 pixel image can be efficiently compressed into a 28 × 7 pixel image. Furthermore, by adjusting the grouping areas, the compression ratio can be tuned from 2× to 28×, providing a highly flexible method for data transmission. By employing the synaptic device characterized by high photoelectric conversion ability and low nonlinearity mapping rules, this compression method achieves a high compression ratio and high quality.

To verify the performance of this compression technique, the preprocessed images were used as input for the neural network described previously. After 50 training epochs with 2× compression, the classification accuracy reached 98.05%, which approaches the accuracy of the initial pattern. When the compression ratio was increased to 28×, significantly enhancing transmission efficiency, the network maintained a respectable accuracy of 74.53%, as illustrated in Figure 5d. These results highlight the device's reliable performance even under ultra-high compression conditions. In addition, the robustness of the weight-transfer model was evaluated by introducing Gaussian noise into the initial images. The noise level, defined as the standard deviation of a Gaussian function, was increased from 10% to 50% [19]. Figure 5b depicts a 4× compressed image with a 20% noise level as a representative example. The testing accuracy for images with noise levels ranging from 10% to 50% in 50 epochs of 4× compressed image is shown in Figure 5e. Meanwhile, Figure S5 shows the accuracy of noisy images with compression ratios from 2 to 28. While a higher noise ratio of 50% initially reduced recognition accuracy in early epochs, the performance eventually converged and reached an accuracy of 86.11%, demonstrating robust noise immunity. Furthermore, the operational capability under low-light conditions is also validated. Under an illumination intensity of 0.84 mW/cm^2, the device continued to exhibit EPSC response with low nonlinearity,

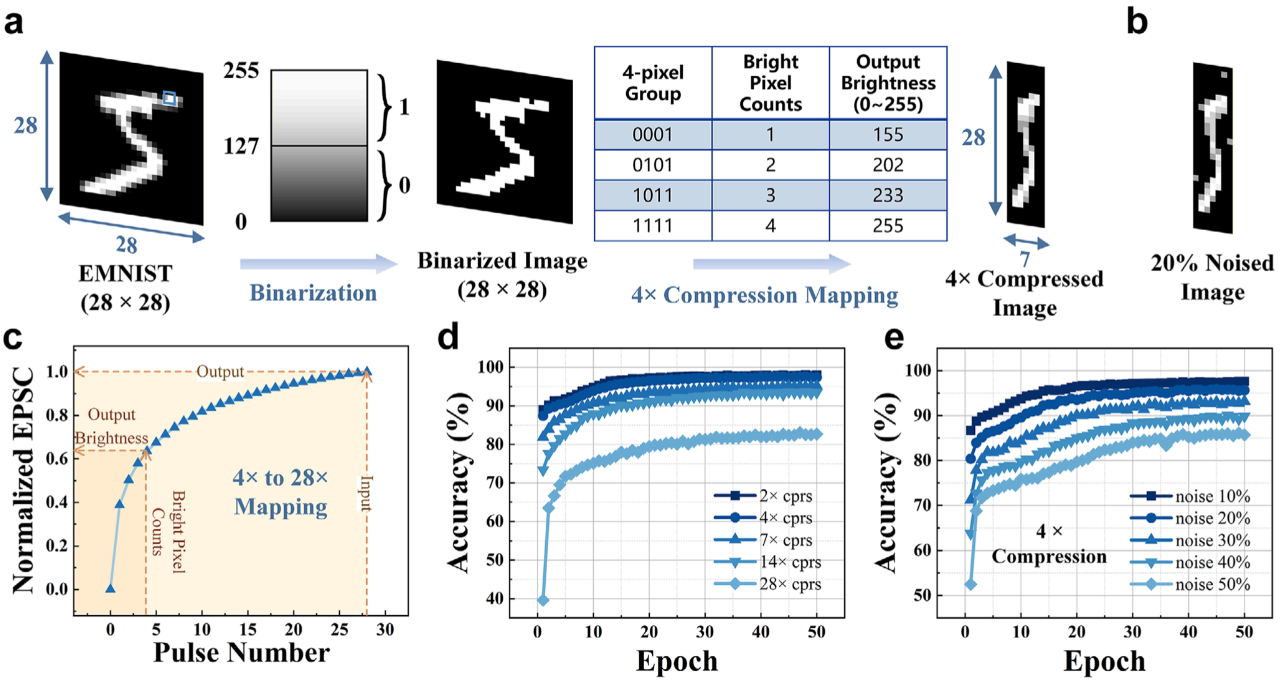

FIGURE 5 | (a) Schematic of image binarization and compression, and images under different compression ratios. (b) Example 4 times compressed image with a noise level of 20%. (c) Mapping the relationship between pulse number and peak EPSC for 2× to 28× compression under 28 consecutive optical pulses (200 ms, 0.5 V). (d) Recognition accuracy as a function of the epoch for 2×, 4×, 7×, 14×, 28× compression. (e) Recognition rates as a function of training epoch with 10%, 20%, 30%, 40%, 50% noise level.

as displayed in Figure S9a. Applying these values into the 2 to 28 times compression process, the highest tested accuracy achieves about 98%, while the recognition accuracy of highly compressed images also maintains, as shown in Figure S9b. Given that the results approach those obtained in previous work, it can be inferred that the image detection and preprocessing capability can be guaranteed over low illumination cases. Based on the unique characteristics of the recessed AlGaN/GaN MOSHEMT, this study achieves an integrated verification of low-power sensing, storage, and computing performance, spanning from data preprocessing to network weight transmission. The device's stable performance under noise interference further confirms its significant potential for future large-scale artificial neural networks.

To investigate the underlying mechanism for the synaptic characteristics, we conducted a detailed analysis of the electrical and material properties. The recessed Al_2O_3/AlGaN/GaN MOSCAP is applied with a more symmetrical structure to evaluate the interface states after etching. Capacitance-voltage characteristics measured with low to high frequency are displayed in Figure S8a and Figure 6a. There is one rising slope of conductance near the V_{th} of the recessed MOSFET. An explicit capacitance dispersion can be observed, indicating the influence of trapped carriers of the interface states. Meanwhile, the G/ω-V peaks in Figure S8b and Figure 6b also prove the existence of traps, as it would increase loss for the device in the range of 1 kHz to 1 MHz. Additional $C-V$ and G/ω-V curves were swept with double mode at the frequency of 100 kHz and 1 MHz, and hysteresis can be observed in positive gate bias, as shown in Figure S7c,d. Setting the voltage range within the rising slope, the frequency-dependent conductance and capacitance curves are presented in Figure 6c and Figure S7e [25]. The interface characteristics of the dielectric layer can be further evaluated from the relationship between measurement frequency and parallel conductance with the following equation [55]:

$$\frac{G}{\omega} = \frac{qD_{it}}{2\omega\tau_{it}} \ln\left[1 + (\omega\tau_{it})^2\right] \tag{7}$$

where D_{it} is the interface trap density, $\omega = 2\pi f$ is the radial frequency, τ_{it} is the characteristic trap response time, and q is the elemental charge. As shown in Figure 6d, the interface trap densities are extracted to ranging from 1.35×10^{12} to 2.96×10^{12} cm^{-2}eV^{-1}, while the corresponding depths of trap energy levels below the conduction band $E_C - E_T$ distribute from 0.4 to 0.6 eV. These results are comparable with the 10^{12} cm^{-2}eV^{-1} amount in previous works [56–58]. The interface states modulate the charge exchange process under optical pulses, providing GaN devices with bionic function and potential in neuromorphic computation.

To further illustrate the performance of the GaN MOSHEMT synaptic device, Table 1 presents the key performance and applications for the neuromorphic system of optically-driven GaN and other reported devices. Our device demonstrates highly symmetric LTP/LTD with strong cycle endurance. While the nonlinearity mainly stems from the carrier trapping-detrapping process, the conduction levels it provides simultaneously enable adaptability for neuromorphic system applications. In the realm of image preprocessing, our device realized a compression method with a compression ratio of up to 28 times, effectively enhancing

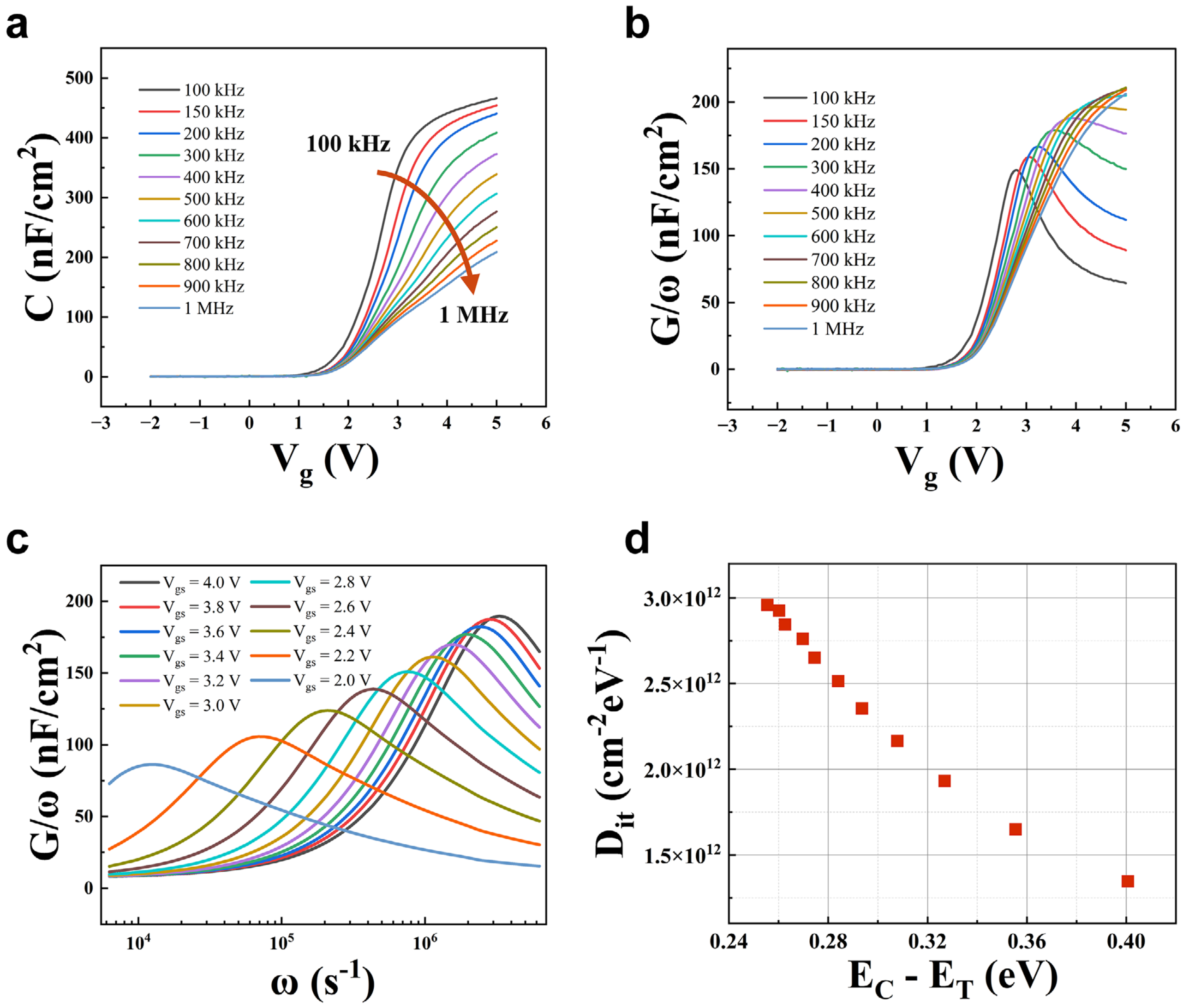

FIGURE 6 | (a) *C–V* characteristics of gate recessed Al_2O_3 MOSCAP from 100 kHz to 1 MHz. (b) *G/ω-V* characteristics from 100 kHz to 1 MHz. (c) Parallel conductance *G/ω* as a function of radial frequency with bias voltage varying from 2.0 to 4.0 V. (D) Interface trap density as a function of the depth of energy level below the conduction band.

transmission efficiency while preserving sufficient image features. Through implementing the synaptic weight modulation into the artificial neural network, we also achieved a competitive accuracy of 98.27%. Additionally, a comparative analysis of the synaptic characteristics about GaN synaptic devices in recent years is listed in Table S2. The recessed-gate structure of our device provides the ability to work at zero gate bias, which efficiently reduces gate energy loss and circuit complexity. The 16.5 pJ energy consumption is also advantageous, representing excellent potential for energy-saving applications. Comprehensive synaptic behaviors are achieved through different modulation types, thereby effectively mimicking biological neurons. Given the CMOS compatibility of Si-substrated AlGaN/GaN devices, it possesses great potential for future large-scale industrialization. Overall, a more comprehensive application consisting of sensing, storage, and computing, which fully exploits the synaptic device, is proposed, paving the way for next-generation hardware-driven computer architecture.

3 | Conclusion

In summary, we have successfully demonstrated and characterized an optoelectronic synaptic transistor based on a recessed-gate AlGaN/GaN MOS-HEMT. Stimulated by 405 nm optical pulses, this synaptic device successfully emulates key biological functions, including EPSC, PPF, STM, and LTM. The recessed-gate architecture allows synaptic operation at zero gate bias, thereby significantly enhancing overall energy efficiency. Under optimized conditions, the energy consumption for a single EPSC event is reduced to 16.5 pJ. The tunability of the EPSC via both drain and gate voltages has been thoroughly documented, providing an additional dimension for the fine-tuning of synaptic weights. Regarding memory consolidation, the transition from STM to LTM can be modulated by adjusting the optical pulse count or frequency, highlighting the potential for repetitive learning and memory. These characteristics further enable the emulation of complex cognitive behaviors, such as step-learning

TABLE 1 | Comparison of key performance and applications for the neuromorphic system.

Material	Nonlinearity of LTP/LTD	Symmetry	Endurance Cycles	Preprocessing Method	Neuromorphic Application	Accuracy (Epoch)	Refs.
Recessed AlGaN/GaN	4.51/4.77	Yes	30	Up to 28 × Compression	Digit Recognition	98.27% (50)	This work
AlGaN/GaN	/	/	/	2 × Compression	/	/	[29]
AlGaN/GaN	/	/	/	/	Digit Recognition	93.4% (50)	[59]
AlScN/p-i-n GaN	0.26	/	500	Image perception and memory	Fingerprint Recognition	93.7% (200)	[9]
p-GaN/(In,Ga)N/GaN	4.21/4.22	Yes	1000	Encrypted communication	Fingerprint Recognition	>90% (100)	[60]
WSe_2-GaN	/	/	/	Image perception and memory	Digit Recognition	96.6% (30)	[61]
GaN NW	/	/	/	/	Digit Recognition	96.0% (20)	[62]
GaN/AlN NW	/	/	20	Contrast Enhancement	Motion classification	95% (20)	[63]
AlGaN/GaN NWs	1.01/2.33	/	/	Contrast Enhancement	Fingerprint Recognition	89% (200)	[64]
Sb_2Te_3/FTO	/	/	/	8 × Compression	/	/	[30]
Ag/SiO_2/Pt	/	/	500	Contrast Enhancement	/	/	[65]
ZnMgO	2.73/3.27	/	/	Encryption Verification	Digit Recognition	95.41% (20)	[38]
MoS_2	0.65/0.7	Yes	1000	/	Digit Recognition	92.2% (125)	[14]
WSe_2	0.31/2.2	/	30	/	Digit Recognition	92.82% (125)	[66]
In_2O_3	0.952/0.985	Yes	100	/	Digit Recognition	94.6% (50)	[67]

and the "learning-forgetting-relearning" behaviors. Additionally, based on the LTD/LTP characteristics, an ANN model incorporating the weight modulation ability achieved an outstanding accuracy of 98.27%. To enhance transmission efficiency, this device leverages its optical detection and processing capabilities to implement a flexible, ultra-high image compression method with a compression ratio of up to 28 times. The model also exhibits high stability in noisy or low-light environments. By consolidating preprocessing and weight modulation into a single hardware platform, this GaN-based synaptic device addresses critical challenges in manufacturing complexity and hardware integration, paving the way for comprehensive, high-performance visual neuromorphic systems.

Acknowledgements

This work was supported by the National Natural Science Foundation of China (Grant No. 52131303). The authors would like to thank ShanghaiTech Material and Device Lab (SMDL) for technical support.

Funding

This work was supported by the National Natural Science Foundation of China (Grant No. 52131303).

Conflicts of Interest

The authors declare no conflicts of interest

Data Availability Statement

The data that support the findings of this study are available from the corresponding author upon reasonable request.

References

1. S. Saha, B. Roy, T. Dey, et al., "Tunable Resistive Switching in $CsPbBr_3$ Nanocrystal-Based Memristors for Artificial Synapse and Neuromorphic Applications," *Advanced Materials Technologies* 10, no. 19 (2025): 00720, https://doi.org/10.1002/admt.202500720.

2. P. Gkoupidenis, D. A. Koutsouras, and G. G. Malliaras, "Neuromorphic Device Architectures With Global Connectivity Through Electrolyte Gating," *Nature Communications* 8, no. 1 (2017): 15448, https://doi.org/10.1038/ncomms15448.

3. L. Zhu, Y. He, C. Chen, Y. Zhu, Y. Shi, and Q. Wan, "Synergistic Modulation of Synaptic Plasticity in IGZO-Based Photoelectric Neuromorphic TFTs," *IEEE Transactions on Electron Devices* 68, no. 4 (2021): 1659–1663, https://doi.org/10.1109/ted.2021.3060687.

4. D. Kudithipudi, C. Schuman, C. M. Vineyard, et al., "Neuromorphic Computing at Scale," *Nature* 637, no. 8047 (2025): 801–812, https://doi.org/10.1038/s41586-024-08253-8.

5. Y. Cao, T. Zhao, C. Zhao, et al., "Advanced Artificial Synaptic Thin-film Transistor Based on Doped Potassium Ions for Neuromorphic Computing via Third-generation Neural Network," *Journal of Materials Chemistry C* 10, no. 8 (2022): 3196–3206, https://doi.org/10.1039/d1tc04827a.

6. C. Zhu, H. Liu, W. Wang, et al., "Optical Synaptic Devices With Ultra-low Power Consumption for Neuromorphic Computing," *Light: Science & Applications* 11, no. 1 (2022): 337, https://doi.org/10.1038/s41377-022-01031-z.

7. T. Zhang, C. Fan, L. Hu, F. Zhuge, X. Pan, and Z. Ye, "A Reconfigurable All-Optical-Controlled Synaptic Device for Neuromorphic Computing Applications," *ACS Nano* 18, no. 25 (2024): 16236–16247, https://doi.org/10.1021/acsnano.4c02278.

8. W. Zhang, B. Gao, J. Tang, et al., "Neuro-Inspired Computing Chips," *Nature Electronics* 3, no. 7 (2020): 371–382, https://doi.org/10.1038/s41928-020-0435-7.

9. Z. Xie, K. Jiang, S. Zhang, et al., "Ultraviolet Optoelectronic Synapse Based on AlScN/p-i-n GaN Heterojunction for Advanced Artificial Vision Systems," *Advanced Materials* 37, no. 19 (2025): 2419316, https://doi.org/10.1002/adma.202419316.

10. L. Zhou, J. Y. Mao, Y. Ren, et al., "Biological Spiking Synapse Constructed From Solution Processed Bimetal Core–Shell Nanoparticle Based Composites," *Small* 14 (2018): 28, https://doi.org/10.1002/smll.201800288.

11. Y. X. Hou, Y. Li, Z. C. Zhang, et al., "Large-Scale and Flexible Optical Synapses for Neuromorphic Computing and Integrated Visible Information Sensing Memory Processing," *ACS Nano* 15, no. 1 (2021): 1497–1508, https://doi.org/10.1021/acsnano.0c08921.

12. H. An, J. S. An, M. Li, Y. Kim, and T. W. Kim, "Electronic Synaptic Devices With High Thermostability Induced by Embedded Tungsten Disulfide Quantum Dots for Machine Learning," *Advanced Electronic Materials* 9, no. 2 (2022): 2200876, https://doi.org/10.1002/aelm.202200876.

13. Z. Yang, Z. Zhang, S. Huo, et al., "Emerging 2D Material-Based Synaptic Devices: Principles, Mechanisms, Improvements, and Applications," *SmartMat* 6, no. 2 (2025): 70005, https://doi.org/10.1002/smm2.70005.

14. Y. Sun, M. Li, Y. Ding, et al., "Programmable Van-Der-Waals Heterostructure-Enabled Optoelectronic Synaptic Floating-Gate Transistors With Ultra-Low Energy Consumption," *InfoMat* 4, no. 10 (2022): 12317, https://doi.org/10.1002/inf2.12317.

15. G. Cao, P. Meng, J. Chen, et al., "2D Material Based Synaptic Devices for Neuromorphic Computing," *Advanced Functional Materials* 31, no. 4 (2021): 2005443, https://doi.org/10.1002/adfm.202005443.

16. N. Ilyas, J. Wang, C. Li, et al., "Nanostructured Materials and Architectures for Advanced Optoelectronic Synaptic Devices," *Advanced Functional Materials* 32, no. 15 (2022): 2110976, https://doi.org/10.1002/adfm.202110976.

17. D. Kimovski, N. Saurabh, M. Jansen, et al., "Beyond Von Neumann in the Computing Continuum: Architectures, Applications, and Future Directions," *IEEE Internet Computing* 28, no. 3 (2024): 6–16, https://doi.org/10.1109/mic.2023.3301010.

18. A. Barri, M. T. Wiechert, M. Jazayeri, and D. A. DiGregorio, "Synaptic Basis of a Sub-second Representation of Time in a Neural Circuit Model," *Nature Communications* 13, no. 1 (2022): 7902, https://doi.org/10.1038/s41467-022-35395-y.

19. Z. Guo, J. Zhang, B. Yang, et al., "Organic High-Temperature Synaptic Phototransistors for Energy-Efficient Neuromorphic Computing," *Advanced Materials* 36, no. 13 (2024): 2310155, https://doi.org/10.1002/adma.202310155.

20. R. Mochida, K. Kouno, Y. Hayata, et al., "A 4 M Synapses Integrated Analog ReRAM Based 66.5 TOPS/W Neural-Network Processor With Cell Current Controlled Writing and Flexible Network Architecture," in *2018 IEEE Symposium on VLSI Technology* (2018): 175–176.

21. X. Zou, J. Yang, Q. Qiao, et al., "Trap Characterization Techniques for GaN-Based HEMTs: a Critical Review," *Micromachines* 14, no. 11 (2023): 2044, https://doi.org/10.3390/mi14112044.

22. P. Wang, Y. Jiang, Y. Gu, et al., "Investigation of Trapping Effects in Schottky Lightly Doped P-GaN Gate Stack Under γ -Ray Irradiation," *Applied Physics Letters* 121, no. 14 (2022): 143501, https://doi.org/10.1063/5.0094090.

23. C. Kai, Y. Wang, X. Liu, et al., "AlGaN/GaN-Based Optoelectronic Synaptic Devices for Neuromorphic Computing," *Advanced Optical Materials* 11, no. 7 (2023): 2202105, https://doi.org/10.1002/adom.202202105.

24. D. Kim, D. Jeong, K. Kim, et al., "Brain-Inspired Topological Surface Modulation for Advanced Nonvolatility in Organic Artificial Synapses," *Small* 21, no. 51 (2025): 05745, https://doi.org/10.1002/smll.202505745.

25. Y. Zhu, H. Du, Y. Zhang, et al., "Dynamic Characteristics of Neutral Beam Etching Enabled Normally-Off Recessed-Gate GaN MOSHEMT," *Power Electronic Devices and Components* 11 (2025): 100087, https://doi.org/10.1016/j.pedc.2025.100087.

26. H. Wang, Y. Tang, Z. Wang, et al., "2D Bi-Doped SnSe Ferroelectric Memristor Integrating All-in-one Sensing-Memory-Computing," *Materials Today Nano* 26 (2024): 100477, https://doi.org/10.1016/j.mtnano.2024.100477.

27. M. Manassi, A. Liberman, W. Chaney, and D. Whitney, "The Perceived Stability of Scenes: Serial Dependence in Ensemble Representations," *Scientific Reports* 7, no. 1 (2017): 1971, https://doi.org/10.1038/s41598-017-02201-5.

28. X. Hua, J. Zheng, X. Han, et al., "Artificial Optoelectronic Synapse With Nanolayered GaN/AlN Periodic Structure for Neuromorphic Computing," *Acs Applied Nano Materials* 6, no. 10 (2023): 8461–8467, https://doi.org/10.1021/acsanm.3c00796.

29. J. Chen, H. Du, H. Qu, et al., "AlGaN/GaN MOS-HEMT Enabled Optoelectronic Artificial Synaptic Devices for Neuromorphic Computing," *APL Machine Learning* 2, no. 2 (2024): 026113, https://doi.org/10.1063/5.0194083.

30. Z. Yu, Z. Wu, W. Xia, et al., "Plasmon-enhanced Sb2Te3/FTO Heterojunction Optoelectronic Synapses for Image Compression Encoding and High-accuracy Recognition," *Applied Physics Letters* 127, no. 22 (2025): 223304, https://doi.org/10.1063/5.0304300.

31. L. Hu, J. Yang, J. Wang, P. Cheng, L. O. Chua, and F. Zhuge, "All-Optically Controlled Memristor for Optoelectronic Neuromorphic Computing," *Advanced Functional Materials* 31, no. 4 (2020): 2005582, https://doi.org/10.1002/adfm.202005582.

32. M. Lee, S. Nam, B. Cho, et al., "Accelerated Learning in Wide-Band-Gap AlN Artificial Photonic Synaptic Devices: Impact on Suppressed Shallow Trap Level," *Nano Letters* 21, no. 18 (2021): 7879–7886, https://doi.org/10.1021/acs.nanolett.1c01885.

33. X. Han, Y. Mo, Y. Wang, X. Yang, J. Wang, and B. Luo, "Amorphous Ga_2O_3/GaN Heterostructure for Ultralow-energy-consumption Optically Stimulated Synaptic Devices," *Applied Physics Letters* 124, no. 1 (2024): 013502, https://doi.org/10.1063/5.0179426.

34. M. T. Hirsch, J. A. Wolk, W. Walukiewicz, and E. E. Haller, "Persistent Photoconductivity in n-type GaN," *Applied Physics Letters* 71, no. 8 (1997): 1098–1100, https://doi.org/10.1063/1.119738.

35. M. S. Mikhailenko, A. E. Pestov, N. I. Chkhalo, et al., "Influence of Ion-Beam Etching by Ar Ions With an Energy of 200–1000 eV on the Roughness and Sputtering Yield of a Single-Crystal Silicon Surface," *Applied Optics* 61, no. 10 (2022): 2825–2833, https://doi.org/10.1364/AO.455096.

36. M. Levin and C. J. Martyniuk, "The Bioelectric Code: an Ancient Computational Medium for Dynamic Control of Growth and Form," *Bio Systems* 164 (2018): 76–93, https://doi.org/10.1016/j.biosystems.2017.08.009.

37. X. Li, H. Sun, M. Ge, et al., "Optically Tunable Synaptic Transistors Based on AlGaN/GaN Heterostructure for Neuromorphic Vision Processing," *Applied Physics Letters* 127, no. 21 (2025): 213301, https://doi.org/10.1063/5.0307178.

38. J. Li, K. Chen, C. Wu, et al., "Low-power Optoelectronic Synaptic Devices With ZnMgO in Deep-ultraviolet Encryption Computation," *Applied Physics Letters* 126, no. 22 (2025): 222104, https://doi.org/10.1063/5.0268617.

39. S. Wen, J. Li, Z. Wang, Z. Zhang, and J. Zhang, "Low-power and High PPF Feature Synaptic Transistors With 3D Interface Based on SnO_2 Nanofibers for Neuromorphic Application," *Applied Physics Letters* 123, no. 4 (2023): 043503, https://doi.org/10.1063/5.0159012.

40. F. Zhou, Z. Zhou, J. Chen, et al., "Optoelectronic Resistive Random Access Memory for Neuromorphic Vision Sensors," *Nature Nanotechnology* 14, no. 8 (2019): 776–782, https://doi.org/10.1038/s41565-019-0501-3.

41. S. Jain, S. Li, H. Zheng, L. Li, X. Fong, and K. W. Ang, "Heterogeneous Integration of 2D Memristor Arrays and Silicon Selectors for Compute-in-memory Hardware in Convolutional Neural Networks," *Nature Communications* 16, no. 1 (2025): 2719, https://doi.org/10.1038/s41467-025-58039-3.

42. J. Fang, Z. Tang, X. C. Lai, et al., "New-Style Logic Operation and Neuromorphic Computing Enabled by Optoelectronic Artificial Synapses in an MXene/Y:HfO_2 Ferroelectric Memristor," *ACS Applied Materials & Interfaces* 16, no. 24 (2024): 31348–31362, https://doi.org/10.1021/acsami.4c05316.

43. Y. Li, Y. Zhong, J. Zhang, et al., "Activity-Dependent Synaptic Plasticity of a Chalcogenide Electronic Synapse for Neuromorphic Systems," *Scientific Reports* 4 (2014): 4906, https://doi.org/10.1038/srep04906.

44. K. Pilarczyk, A. Podborska, M. Lis, M. Kawa, D. Migdal, and K. Szaciłowski, "Synaptic Behavior in an Optoelectronic Device Based on Semiconductor-Nanotube Hybrid," *Advanced Electronic Materials* 2, no. 6 (2016): 1500471, https://doi.org/10.1002/aelm.201500471.

45. F. Wu, X. Zhang, K. Chen, et al., "High-Performance Solar-blind Optoelectronic Synaptic Device Based on N-Doped Ga_2O_3 Nanowire Network for Neuromorphic Computing," *Journal of Applied Physics* 138, no. 22 (2025): 223106, https://doi.org/10.1063/5.0307144.

46. Y. Mo, B. Luo, H. Dong, and B. Hou, "Light-Stimulated Artificial Synapses Based on Si-doped GaN Thin Films," *Journal of Materials Chemistry C* 10, no. 36 (2022): 13099–13106, https://doi.org/10.1039/d2tc02168d.

47. J. Shi, C. Chen, X. Li, H. Chen, H. Lin, and Z. Chen, "Optoelectronic Synaptic Transistors via Adding Insulator Into Semiconductor for Brain-Inspired Computing," *IEEE Transactions on Electron Devices* 71, no. 11 (2024): 6989–6995, https://doi.org/10.1109/ted.2024.3454033.

48. T. Feng, H. Xu, Y. Yang, et al., "Organic Synaptic Transistors Based on C8-BTBT/PMMA/PbS QDs for UV to NIR Face Recognition Systems," *Nano Letters* 25, no. 9 (2025): 3637–3645, https://doi.org/10.1021/acs.nanolett.5c00032.

49. Y. Choi, S. Oh, C. Qian, J. H. Park, and J. H. Cho, "Vertical Organic Synapse Expandable to 3D Crossbar Array," *Nature Communications* 11, no. 1 (2020): 4595, https://doi.org/10.1038/s41467-020-17850-w.

50. P. Y. Chen, X. Peng, and S. Yu, "NeuroSim+: An integrated device-to-algorithm framework for benchmarking synaptic devices and array architectures," in *2017 IEEE International Electron Devices Meeting* (2017): 6.1.1–6.1.4.

51. S. Seo, S. H. Jo, S. Kim, et al., "Artificial Optic-neural Synapse for Colored and Color-mixed Pattern Recognition," *Nature Communications* 9, no. 1 (2018): 5106, https://doi.org/10.1038/s41467-018-07572-5.

52. C. Qian, S. Oh, Y. Choi, et al., "Solar-stimulated Optoelectronic Synapse Based on Organic Heterojunction With Linearly Potentiated Synaptic Weight for Neuromorphic Computing," *Nano Energy* 66 (2019): 104095, https://doi.org/10.1016/j.nanoen.2019.104095.

53. D. Li, "The MNIST Database of Handwritten Digit Images for Machine Learning Research [Best of the Web]," *IEEE Signal Processing Magazine* 29, no. 6 (2012): 141–142, https://doi.org/10.1109/msp.2012.2211477.

54. N. Carlini and D. Wagner, "Towards Evaluating the Robustness of Neural Networks," in *2017 IEEE Symposium on Security and Privacy* (2017): 39–57.

55. R. Engel-Herbert, Y. Hwang, and S. Stemmer, "Comparison of Methods to Quantify Interface Trap Densities at Dielectric/III-V Semiconductor Interfaces," *Journal of Applied Physics* 108, no. 12 (2010): 124101, https://doi.org/10.1063/1.3520431.

56. S. Yang, Z. Tang, K.-Y. Wong, et al., "Mapping of interface traps in high-performance Al_2O_3/AlGaN/GaN MIS-heterostructures using frequency- and temperature-dependent C-V techniques," in *2013 IEEE International Electron Devices Meeting* (2013): 6.3.1–6.3.4.

57. T. L. Wu, D. Marcon, B. Bakeroot, et al., "Correlation of Interface States/Border Traps and Threshold Voltage Shift on AlGaN/GaN

Metal-Insulator-Semiconductor High-electron-mobility Transistors," *Applied Physics Letters* 107, no. 9 (2015): 093507, https://doi.org/10.1063/1.4930076.

58. J. L. Zhang, L. He, L. Li, et al., "High-Mobility Normally OFF Al_2O_3/AlGaN/GaN MISFET with Damage-Free Recessed-Gate Structure," *IEEE Electron Device Letters* 39, no. 11 (2018): 1720–1723, https://doi.org/10.1109/Led.2018.2872637.

59. L. Qian, X. Hong, W. Qian, et al., "Gate-tunable Synaptic Weight Modulation in AlGaN/GaN HEMT Optoelectronic Synapses for Neuromorphic Computing," *Materials Science in Semiconductor Processing* 206 (2026): 110446, https://doi.org/10.1016/j.mssp.2026.110446.

60. M. Jiang, Y. Zhao, L. Bian, et al., "Realizing Bidirectional Photocurrent in Monolithic Dual-Mode Device for Neuromorphic Vision and Logically-Encrypted Transmission," *Advanced Functional Materials* 35, no. 19 (2024): 2416288, https://doi.org/10.1002/adfm.202416288.

61. Z. Su, Y. Yan, M. Sun, et al., "Broadband Artificial Tetrachromatic Synaptic Devices Composed of 2D/3D Integrated WSe_2 -GaN-Based Dual-Channel Floating Gate Transistors," *Advanced Functional Materials* 34 (2024): 33, https://doi.org/10.1002/adfm.202316802.

62. X. Gu, Z. Liu, J. Zhang, X. Huang, Y. Zhao, and L. Bian, "Controllable and Cost-Efficient Three-Terminal GaN Nano-Synapse for Brain-Inspired Computing," *Small* 22, no. 27 (2026): 14447, https://doi.org/10.1002/smll.202514447.

63. Z. Gao, X. Ju, H. Yu, et al., "Ultrathin Gallium Nitride Quantum-Disk-in-Nanowire-Enabled Reconfigurable Bioinspired Sensor for High-Accuracy Human Action Recognition," *Nano-Micro Letters* 18, no. 1 (2025): 54, https://doi.org/10.1007/s40820-025-01888-w.

64. Y. Zhang, Y. Huang, C. Huang, et al., "Plasma-Engineered AlGaN/GaN Optoelectronic Synapses for Low-Power Neuromorphic Computing," *Advanced Optical Materials* 13, no. 13 (2025): 2403370, https://doi.org/10.1002/adom.202403370.

65. L. Wu, Z. Wang, B. Wang, et al., "Emulation of Biphasic Plasticity in Retinal Electrical Synapses for Light-Adaptive Pattern Pre-processing," *Nanoscale* 13, no. 6 (2021): 3483–3492, https://doi.org/10.1039/d0nr08012h.

66. J. Sung, S. W. Kim, D. Lee, S. Moon, E. Lee, and H. H. Kim, "Co-Stimuli-Driven 2D WSe_2 Optoelectronic Synapses for Neuromorphic Computing," *Small* 21, no. 31 (2025): 2504024, https://doi.org/10.1002/smll.202504024.

67. H. Qiu, D. Hao, H. Li, et al., "Transparent and Biocompatible In_2O_3 Artificial Synapses With Lactose–Citric Acid Electrolyte for Neuromorphic Computing," *Applied Physics Letters* 121, no. 18 (2022): 183301, https://doi.org/10.1063/5.0124219.

Supporting Information

Additional supporting information can be found online in the Supporting Information section.

Supporting File: admt71128-sup-0001-SuppMat.docx.